Scilight

Photochemistry and Spectroscopy
https://www.sciltp.com/journals/ps

Article

Investigation of Dielectric Behavior, Diffuse Phase Transition, and Optical Band Gap in Polycrystalline $KSr_{0.5}Fe_2O_4$ Ceramics

Mohamed Mounir [1], Ibtihel Soudani [1], Samia Aydi [2], Abderrazek Oueslati [2] and Abdelhedi Aydi [1,*]

[1] Laboratory of Multifunctional Materials and Applications (LaMMA), LR16ES18, Faculty of Sciences of Sfax, University of Sfax, BP 1171, Sfax 3000, Tunisia
[2] Laboratory for Spectroscopic Characterization and Optics of Materials (LaSCOM), LR17ES09, Faculty of Sciences, University of Sfax, BP 1171, Sfax 3000, Tunisia
* Correspondence: aydi_abdelhedi@yahoo.fr

How To Cite: Mounir, M.; Soudani, I.; Aydi, S.; et al. Investigation of Dielectric Behavior, Diffuse Phase Transition, and Optical Band Gap in Polycrystalline $KSr_{0.5}Fe_2O_4$ Ceramics. *Photochemistry and Spectroscopy* **2025**, *1*(1), 4. https://doi.org/10.53941/ps.2025.100004

Received: 4 November 2025
Revised: 10 December 2025
Accepted: 12 December 2025
Published: 23 December 2025

Abstract: This study investigates the dielectric phase transition and optical properties of polycrystalline KSFO ($KSr_{0.5}Fe_2O_4$). The temperature dependence of the dielectric constant reveals clear phase-transition behavior. Diffuse phase characteristics are evaluated using the modified Curie–Weiss law and Lorentzian analysis. Dielectric analysis as a function of temperature indicates a ferroelectric–paraelectric (FE–PE) transition, evidenced by a pronounced increase in the real part of the permittivity near 480 K. At lower temperatures, the material exhibits high dielectric permittivity and low dielectric loss, highlighting its potential for energy storage applications. Optical measurements yield a direct band gap of 2.10 eV, confirming the semiconducting nature of the KSFO ceramic. Overall, these results suggest that KSFO is a promising candidate for multifunctional device applications.

Keywords: dielectric permittivity; ferroelectric-paraelectric transition; modified Curie-Weiss law; semiconducting nature, applications

1. Introduction

Research on relaxor ferroelectric materials has advanced steadily. Owing to their outstanding dielectric and electromechanical properties, these materials are widely used in microelectronics, particularly in capacitors and actuators [1]. Ferrite-based materials are also widely used in such devices. As an important class of oxides, ferrites have attracted considerable interest because of their multifunctional properties and broad use in electrical systems, sensors, transformers, microwave technologies, and data storage [2,3]. They are notable for their high electrical resistivity and magnetic permeability [4]. In addition, their low dielectric and magnetic losses make them suitable for devices such as transformers [5], microwave absorption [6], data-storage media [7], magnetic recording and sensing [8], magnetic refrigeration technologies [9], and optoelectronics components [10,11].

According to Khan et al., the notable dielectric performance of ferrites with high permittivity and low loss, is similar to chromites and cobaltites [12]. This behavior depends on factors such as chemical composition, synthesis route, dopants, crystallite size, and sintering conditions [13,14]. Critical dielectric parameters include the dielectric constant (permittivity, ε'), which reflects charge-storage capability, and the dissipation factor, which represents dielectric loss. Together, these parameters govern ferrite performance in targeted applications. Various methods can be used to synthesize these materials; among them, the solid-state reaction route is straightforward, economical reliable, and it is employed here to prepare KSFO [15,16].

Ferrites, which belong to the oxide-ceramic family, consist primarily of iron oxide (Fe_2O_3) combined with small amounts of transition metals (e.g., Zn, Co, Ni, and Mn) to tailor their properties. Iron oxide contributes

ferrimagnetic behavior while maintaining electrical insulation [17]. Strontium ferrite ($SrFe_2O_4$) can exhibit mesoporous structures, high surface area, and oxygen vacancies partly associated with the large ionic radius of Sr^{2+} [15,18,19]. Doping particularly with alkali ions (K, Na, Li) is a proven approach to enhance structural, optical, electrical, and dielectric properties. Although strontium ferrites are well-researched, specifically addressing the effects of potassium (K) doping remains limited.

Our earlier electrical study provided initial insights into conduction mechanisms, but it was insufficient to fully assess the material's multifunctional capabilities and application potential [20]. Therefore, the present work complements the previous electrical results with a detailed investigation of the optical properties. We focus on relating dielectric behavior to temperature-driven changes in the dielectric constant, thereby providing a broader view of charge transport, polarization dynamics, and energy-storage potential. Application of the Curie–Weiss and modified Curie–Weiss laws provides quantitative insight into the dielectric response and supports the material's applicability. In addition, UV-Vis absorption measurements are used to probe the optical characteristics.

2. Experimental Details

2.1. Preparation Method

The KSFO ceramic was synthesized using the conventional solid-state reaction technique, as fully described previously [20]. High-purity powders of K_2CO_3, Sr_2CO_3, and Fe_2O_3 (Aldrich 99.9%) were weighed according to their stoichiometric ratios. The resulting mixture was thoroughly ground and then compressed into a pellet (~1 mm thick) to ensure compositional homogeneity and facilitate elemental diffusion. The pellet was subsequently to calcination at two temperatures (T_1 = 1123 K and T_2 = 1323 K) for 8 h each. The final processing step consisted of multiple sintering cycles at 1373 K for 3 hours, with intermediate grinding and pelletizing, resulting in a pure, homogeneous, and densely crystallized product. Figure 1 illustrates the synthesis process of the LKPO sample.

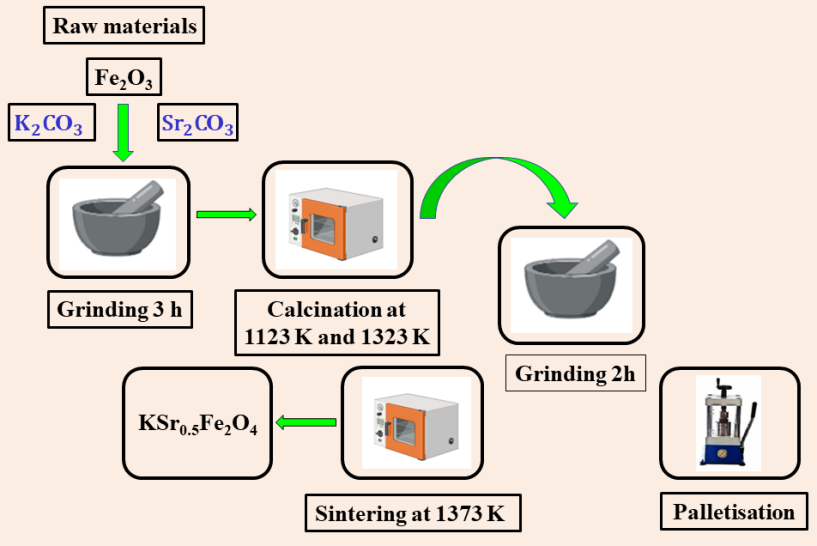

Figure 1. Schematic synthesis procedure of KSFO.

2.2. Characterization Methods

For dielectric measurements, gold electrodes were deposited on both faces of the disk-shaped samples. The real part of the relative dielectric permittivity (ε_r') was measured using an Agilent 4284 A impedance analyzer (from 20 Hz^{-1}·MHz) across 410–510 K.

Optical properties were evaluated at room temperature using a Shimadzu UV-visible spectrophotometer (200–800 nm). The UV–visible absorption spectra were used to determine the optical band gap (Eg) and to confirm the semiconducting nature of the material.

3. Results and Discussion

3.1. Structural and Microstructural Characterization

Figure 2 shows the X-ray diffractogram patterns of a KSFO at room temperature. The diffraction peaks were indexed to the monoclinic structure with the P21/n space group. A single-phase formation was confirmed without detectable secondary phases. All structural parameters from the Rietveld refinement are reported in Table 1 [20].

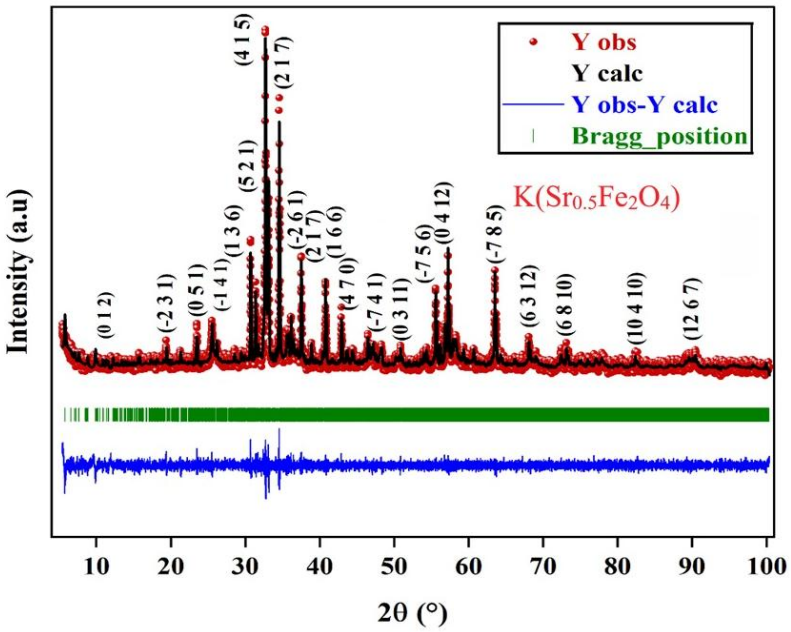

Figure 2. XRD pattern of KSFO.

Table 1. Rietveld refined parameters for KSFO.

Formula	KSFO (Room Temperature)
Crystalline system	Monoclinic
Space group	P 2_1/n
Lattice parameters	
a	15.278 Å
b	17.664 Å
c	20.734 Å
α = β and γ	90° and 91.658°
Reliability factors	
$R_P/R_{WP}/R_{exp}$	26.5%/28.4%/25.70%
χ^2	1.22

Scanning electron microscopy (SEM) imaged the sample morphology (Figure 3). As reported earlier, the average grain size is relatively large, approximately 5 μm [20].

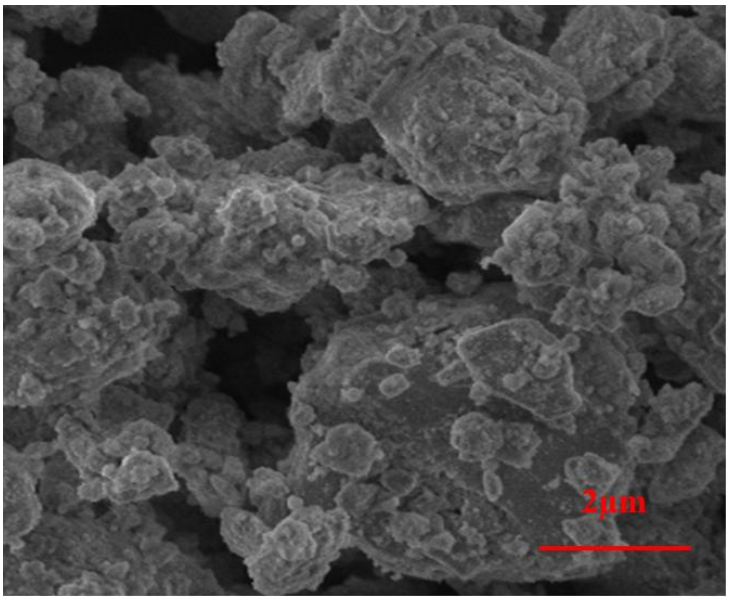

Figure 3. SEM image of KSFO at a scale of 2 μm.

3.2. Dielectric Properties

The dielectric response of KSFO was investigated to determine its ferroelectric phase transition temperature and to elucidate its relaxation mechanisms. Figure 4a,b illustrate the temperature- and frequency-dependent behavior of the dielectric constant (ε′) and loss tangent (tan δ), revealing characteristic relaxor behavior. Dielectric properties remain stable at low temperatures. The dielectric constant increases gradually with temperature up to 450 K, followed by a sharp rise that mirrors the behavior of the loss tangent, suggesting the occurrence of a phase transition or relaxation process. A frequency-dependent peak in ε′(*T*) observed between 450 and 500 K signifies a ferroelectric–paraelectric transition. Compared with relaxors materials such as $Ni_{0.6}Zn_{0.4}Al_{0.5}Fe_{1.5}O_4$ (ε′ = 130) [21], the present ceramic exhibits a very high permittivity, reaching $\varepsilon'_m \approx 3400$.

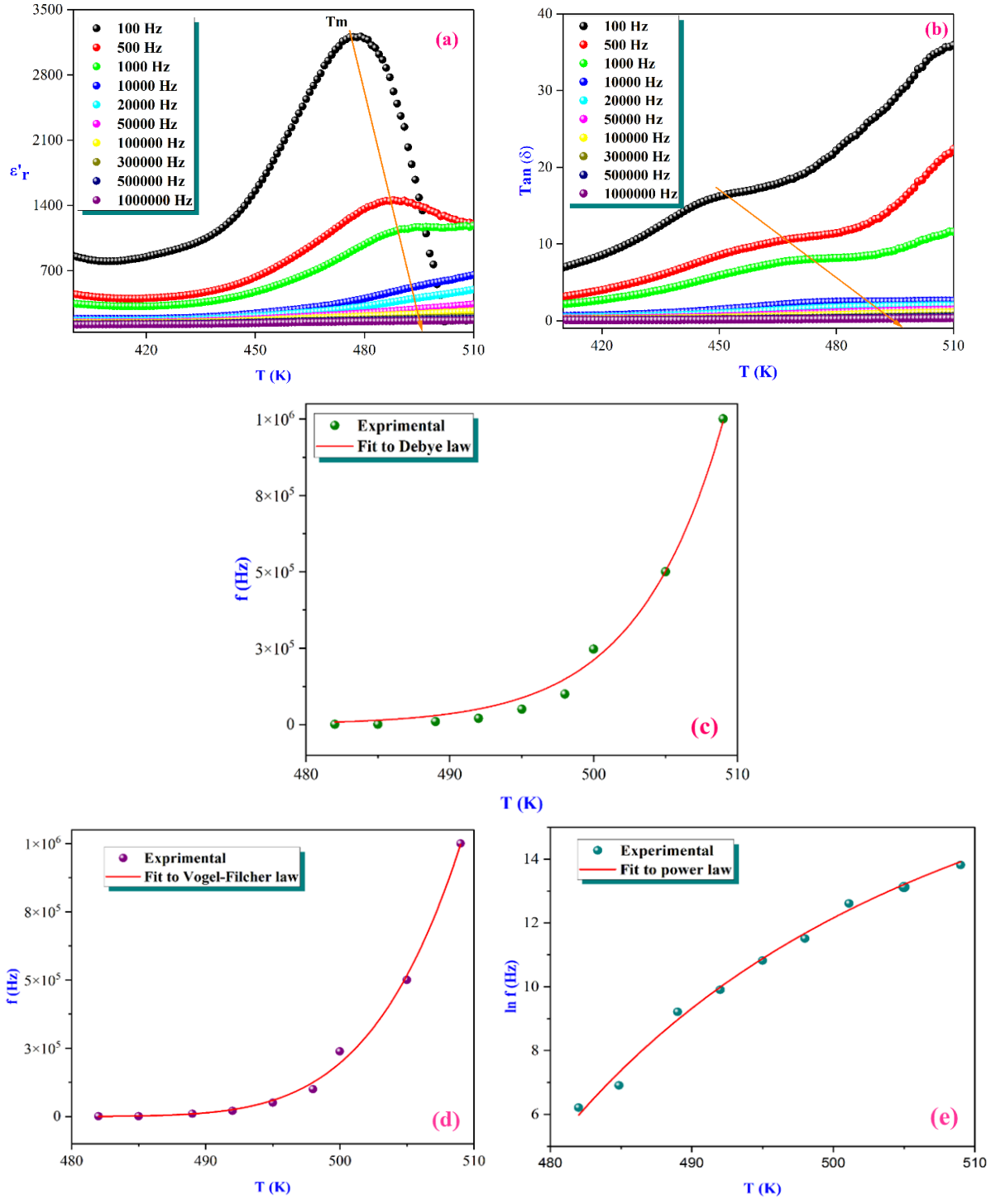

Figure 4. Temperature dependence of dielectric (ε′) (**a**) Temperature dependence of the dielectric loss (tan δ) at various frequencies (**b**) Fitting to the dielectric relaxation data of the sample of (**c**) Debye, (**d**) Vogel-Fulcher, and (**e**) Power model.

The frequency dependence of the permittivity peak temperature (T_m) was analyzed using the Debye and the Vogel-Fulcher (V-F) models.

The Debye model is expressed as [22]:

$$f = f_0 \exp(-\frac{E_a}{K_B T_m}) \quad (1)$$

where E_a is the activation energy for the jump, f_0 is the pre-exponential factor, Tm denotes the temperature at which the real part of the dielectric permittivity, ε′(T), reaches its maximum value, and K_B is the Boltzmann constant. Compared to the fit (Figure 4c), the unphysical higher values $f_0 = 5.09 \times 10^{12}$ Hz and E_a= 1.54 eV are calculated [23,24].

In the solid systems, the attempt frequency f_0 falls between 10^{12} and 10^{13} Hz, which is higher than expected for non-interacting dipoles. This observation suggests that dipole-dipole interactions are significant and that the Debye model alone is insufficient to fully describe their behavior. The limitations of the Debye model in describing the dipole dynamics point to the influence of considerable dipole-dipole interactions. Consequently, a more detailed analysis of the relaxation behavior was undertaken. Accordingly, the experimental data were fitted using the Vogel–Fulcher equation, which describes behavior similar to that observed in cluster glass systems.

The relationship can be approximated by [25]:

$$f = f_0 \exp(-\frac{E_a}{K_B T_m - T_{VF}}) \quad (2)$$

T_{VF} is the freezing temperature. The V-F model provided more reasonable parameters: Ea = 0.505 eV, T_{VF} = 471.84 K, and $f_0 = 6.555 \times 10^9$ Hz (Figure 4d).

These values (T_{VF} and E_a) are consistent with thermally activated polarization fluctuations and suggest a diffuse phase transition (DPT). The activated dynamic scaling law [26]:

$$\ln f = \ln f_0 - U(T - T_c)^{zv} \quad (3)$$

Fitted well (Figure 4e), giving $f_0 = 6.7 \times 10^8$ Hz, T_C = 472.7 K, zv = 1.24, and U = 6185 K. The exponent zv > 1 aligns with the 2D Ising model. In the parameteric region, the dielectric constant typically follows the Curie–Weiss law [27]:

$$\frac{1}{\varepsilon'} = \frac{T - T_C}{C} \quad (4)$$

where ε′ is the dielectric constant, C is the Curie-Weiss constant, and T_C is the Curie-Weiss temperature.

Fitting the inverse relative permittivity at 500 Hz (Figure 5a) yielded $C = 2.563 \times 10^4$ and T_C = 483 K, respectively. Deviation from this law, quantified by $\Delta T_m = T_{Dev} - T_m$ = 17 K, evidences DPT behavior [28].

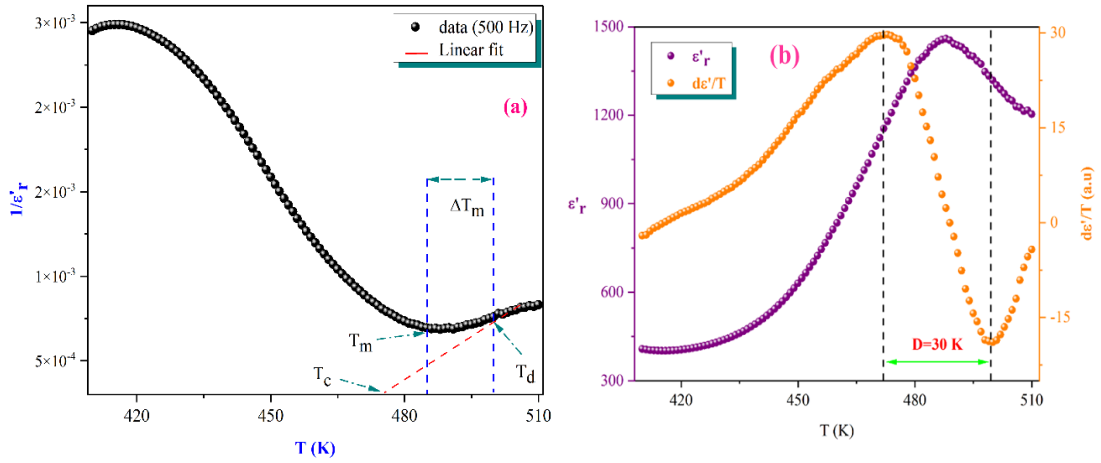

Figure 5. (**a**) The inverse of dielectric constant ($1/\varepsilon_r'$) as a function of the temperature of the KSFO at 500 Hz (**b**) Value of the diffuseness degree for the KSFO ferrite sample.

The diffuseness (γ) was calculated using [29]:

$$\frac{1}{\varepsilon'_r} - \frac{1}{\varepsilon'_{max}\frac{(T - T_m)^\gamma}{C}} \quad T > T_m \tag{5}$$

The diffuseness coefficient γ allows understanding of the character of the phase transition; C is a constant quantity, and ε'_{max} is the peak dielectric permittivity at temperature T_m. The Values of the diffuseness exponent γ between 1 and 2 suggest the presence of a partially diffuse phase transition. In the framework established by Uchino et al., γ ≈ 1 denotes a conventional ferroelectric transition, whereas γ ≈ 2 is indicative of a fully ideal relaxor ferroelectric nature [29].

Figure 6 displays the plot of ln $(\frac{1}{\varepsilon'_r} - \frac{1}{\varepsilon'_{max}})$ as a function of ln (T − T_m) at 100 Hz. The slope of the linear fit to the experimental data allows for determining the values of the γ diffusion factor. We noted that γ is equal to 1.98. This result indicates the existence of an ideal relaxor behavior.

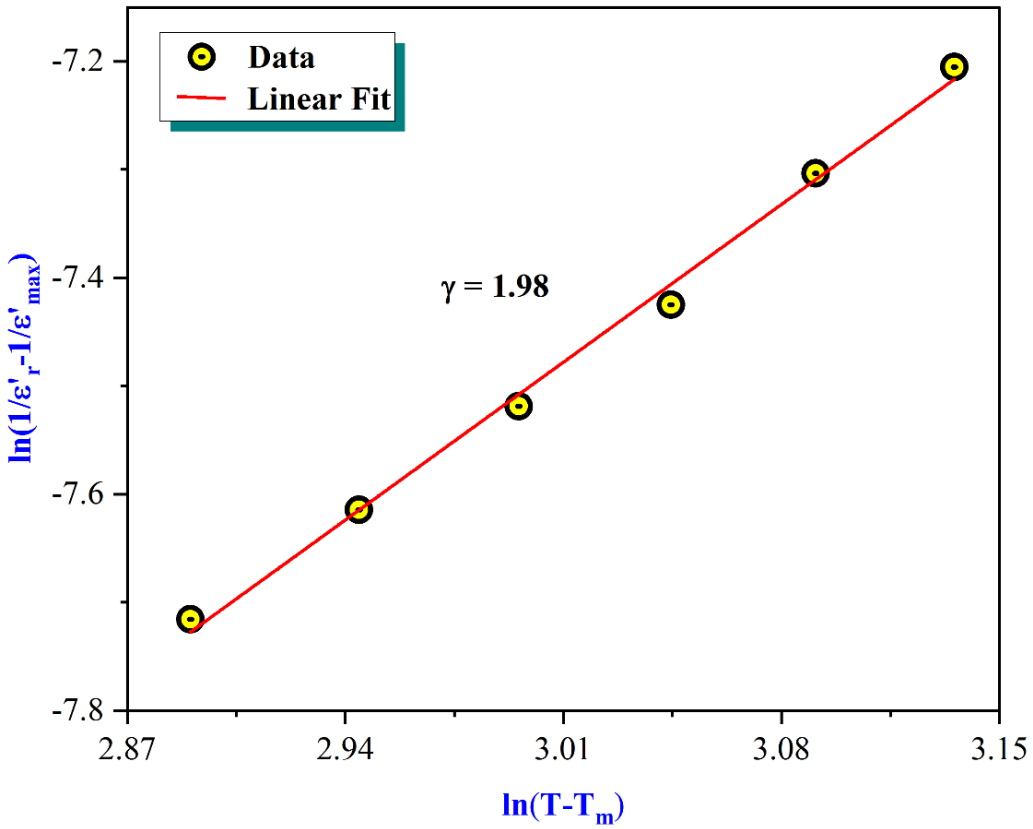

Figure 6. Variation of ln (1/ε'_r − 1/ε'_{max}) as a function of ln (T − T_m).

To evaluate the frequency-dependent dispersion in the dielectric properties ε'_m and T_m, specific empirical relaxation parameters are introduced [30].

$$\Delta\varepsilon' = \frac{\Delta\varepsilon'_m}{\varepsilon'_m} = \frac{\varepsilon'_{m(100\ Hz)} - \varepsilon'_{m(1{,}000{,}000\ Hz)}}{\varepsilon'_{m(100\ Hz)}} \times 100 \tag{6}$$

$$\Delta T_{res} = T_{m(1{,}000{,}000\ Hz)} - T_{m(100\ Hz)} \tag{7}$$

The values calculated of ΔT_{res} = 34 K and Δε′ =79.5% serve as indicators of a relaxor state and a significant permittivity dispersion. The diffuseness degree D (D = 30 K, Figure 5b) defines the temperature interval over which changes in the volume fraction of polar microscopic regions occur as new polar regions emerge. The consistency between D, the diffuseness exponent γ and the temperature shift ΔTm confirms the relaxor-like nature of the KSFO ferrite sample.

Moreover, the Lorentz empirical formula, widely employed to describe the temperature dependence of dielectric permittivity in relaxor ferroelectrics, particularly on the high-temperature side of the permittivity maximum, can be expressed in the following general form:

$$\frac{\varepsilon'_A}{\varepsilon'} = 1 + \frac{(T - T_A)^2}{2\delta_A^2} \quad (8)$$

where ε'_A represents the magnitude of the Lorentz peak, T_A ($T_A \neq T_m$) corresponds to the temperature at the peak position, and δ_A denotes the diffuseness parameter characterizing the relaxor behavior. The best-fit parameters obtained from the experimental data are ε'_A = 3634, T_A = 477 K, and δ_A = 52.59 K for T < Tm, while for T > T_m, ε'_A = 3614, T_A = 498 K, and δ_A = 32.45 K. As shown in Figure 7, the fitting curves exhibit good agreement with the experimental data, particularly near and above T_m. Notably, the pronounced variation of δ_A between the low- and high-temperature regions suggests the coexistence of two distinct polarization mechanisms in the present system. Nevertheless, the obtained δ_A values remain comparable to those reported for other relaxor ceramics [31,32], confirming the strong relaxor dispersion behavior of the sample.

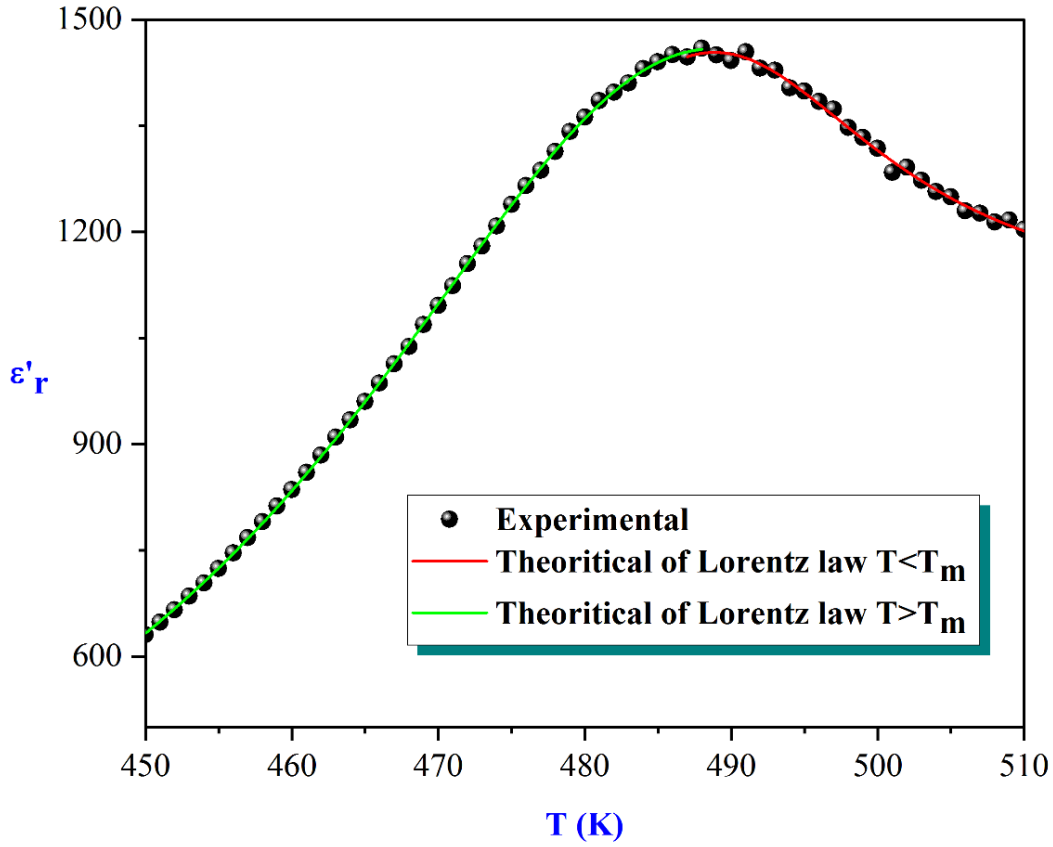

Figure 7. Experimental and fitted dielectric data as a function of temperature using the Lorenz type.

3.3. Optical Properties

Optical analyses are commonly performed to evaluate the luminous efficiency and overall quality of the compound. The photo-absorption properties of the material are investigated using UV–visible diffuse reflectance spectroscopy. The spectra recorded at room temperature over the wavelength range of 200–800 nm is presented in Figure 8. According to previous reports on ferrites, the absorption can be attributed either to Fe^{3+} electronic transitions (from $3d^5$ to $3d^44s^1$) or to photoexcitation processes, in which electrons are promoted from the valence band (VB, O 2p states) to the conduction band (CB, Fe 3d states) upon visible-light excitation [33]. The optical bandgap (E_g) value of KSFO is obtained using the Kubelka–Munk function and the Tauc plot [34].

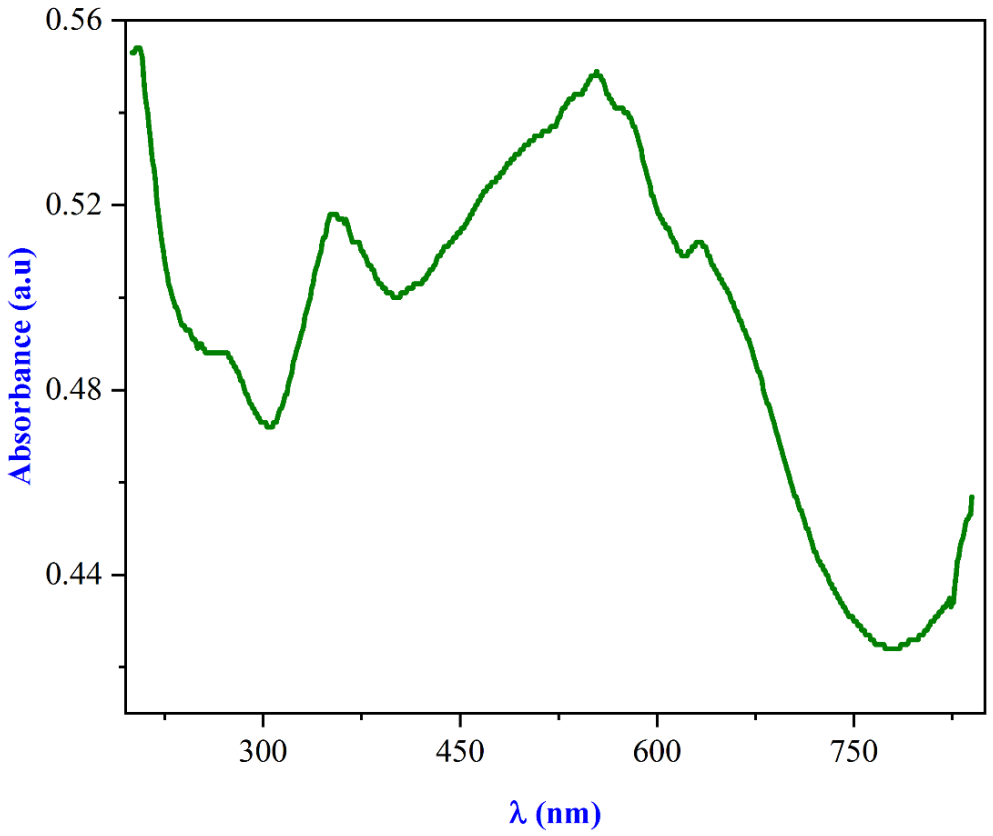

Figure 8. UV-Vis absorbance spectrum of the KSFO in the range 200–800 nm.

On the one hand, the Kubelka–Munk function is as follows:

$$F(R) = \frac{(1-R)^2}{2R} = \frac{\alpha}{s} \quad (9)$$

where R is the reflection factor, a is the absorption coefficient, and s is a scattering factor.

The relation used for the determination of the optical band energy, we utilize the Tauc method [35]:

$$\alpha h\nu = \alpha_0 (h\upsilon - E_g)^n \quad (10)$$

where hν is the photon energy, α_0 is the optical constant, and n equals 1/2 or 2 for direct or indirect transition, respectively. KSFO shows a direct band gap like other compounds belonging to the ferrite family [33,36,37].

Figure 9 presents the plot of $(\alpha h\nu)^2$ as a function of photon energy (hν). The optical energy band gap for the direct transition E_{gd} at 2.10 eV is determined from this plot. The optical bandgap of the sample is 2.10 eV, which falls in the range of a semiconductor bandgap. The semiconducting nature of this material makes it a promising candidate for photodetectors and photovoltaics applications [36].

To ensure the value of the energy gap, the curve of 1/R dR/dλ versus wavelength is plotted in Figure 10. This provides evidence for the presence of an optical bandgap at 2.10 eV, which is close to the value obtained by Kubelka–Munk. Thereby, we confirmed the direct type of transition and the semiconducting nature of the synthesized ceramic.

The band gap value of 2.15 eV exceeds the minimum energy required for water splitting (E > 1.23 eV), which facilitates more efficient charge separation and enhances the photocatalytic activity under visible light due to the material's strong absorption in the visible region [38].

To check the transition mode of the optical strip for our compound, the following equation is used to express:

$$Ln(\alpha h\nu) = Ln\alpha_0 + n\, Ln(h\nu - E_g) \quad (11)$$

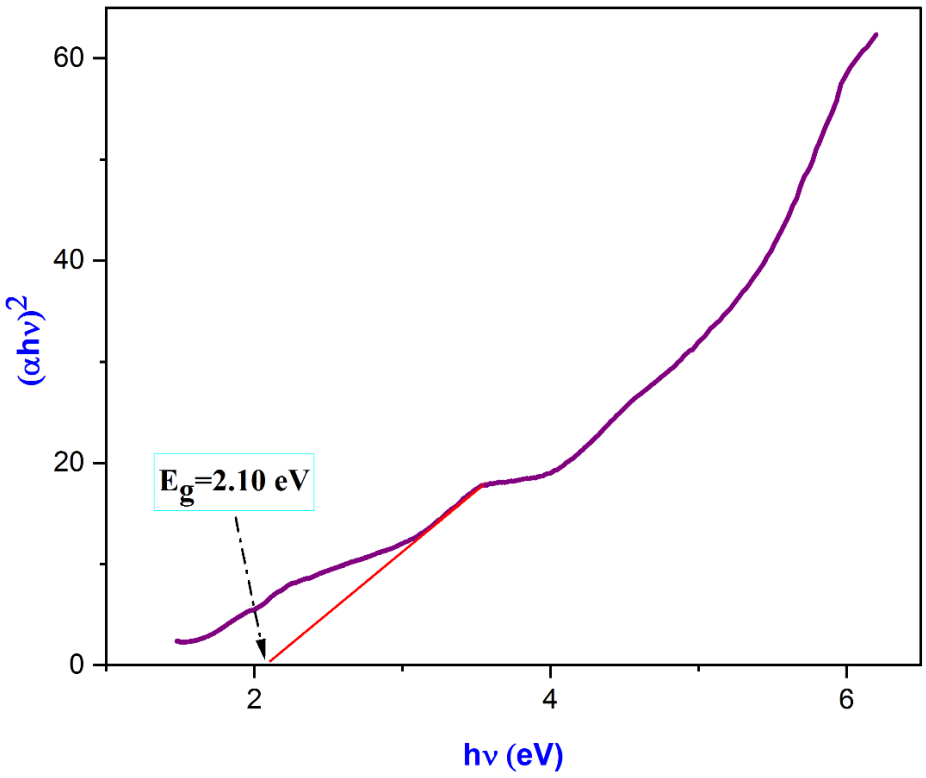

Figure 9. The Tauc plot for the determination of the bandgap value for the KSFO compound.

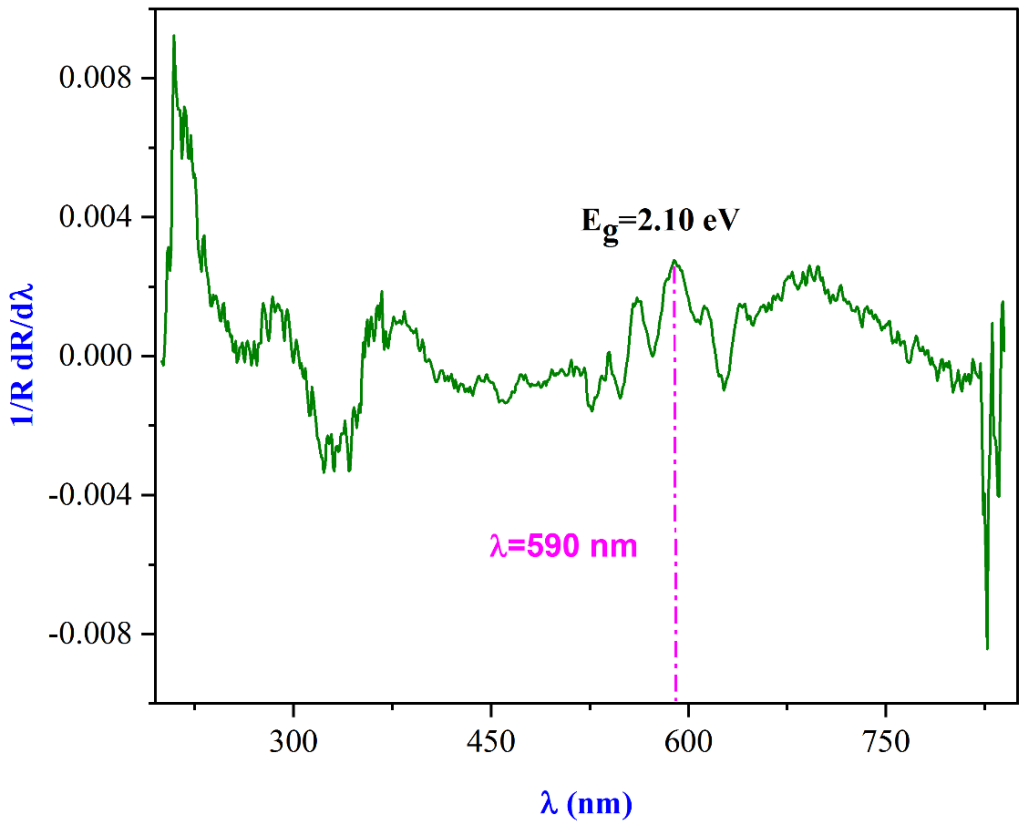

Figure 10. The plot of 1/R dR/dλ versus wavelength (λ).

Figure 11 shows the evolution of Ln (αhν) against Ln (hν − 2.10) for KSFO. This curve demonstrates a straight line whose slope gives the power factor (n = 0.7), which is close to ½, confirming the direct semiconductor behavior of KSFO. This obtained value is close to the value obtained by the Marotti method. These results indicate

that the compound possesses a well-defined band gap with semiconducting behavior [39,40], further supporting its potential for photovoltaic and optoelectronic devices [41].

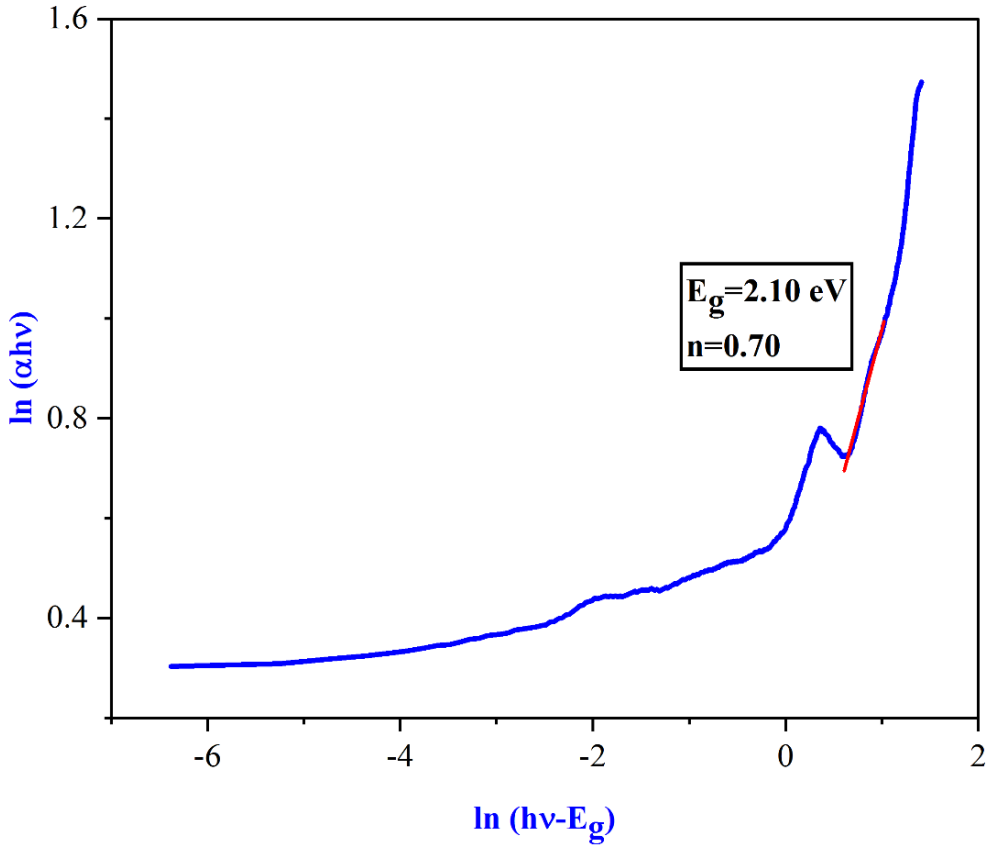

Figure 11. Evolution of Ln (αhν) against Ln (hν − E_g) for the KSFO compound.

4. Conclusions

In summary, the dielectric and optical properties of KSFO ceramics synthesized via the solid-state route were systematically investigated. The ceramic exhibits a high dielectric constant, low dielectric loss, and a high Curie temperature (TC), highlighting its potential for spintronic and multifunctional device applications. The frequency- and temperature-dependent dielectric behavior reveals a relaxor ferroelectric transition occurring near 500 K. The optical band gap, determined using the Tauc model, was found to be 2.10 eV, confirming the semiconducting nature of the material. The enhanced dielectric and optical performance suggest that the KSFO ceramic is a promising candidate for applications in memory devices, photocatalysis, and solar energy conversion.

Author Contributions

I.S.: conceptualization, methodology, software; M.M.: data curation, writing—first draft; S.A.: visualization, investigation and supervision; A.O.: software, validation; A.A.: writing—review and corrections. All authors have read and agreed to the published version of the manuscript.

Funding

This research received no external funding.

Institutional Review Board Statement

Not applicable.

Informed Consent Statement

Not applicable.

Data Availability Statement

Data will be made available on request.

Conflicts of Interest

The authors declare no conflict of interest.

Use of AI and AI-Assisted Technologies

No AI tools were used in this study.

References

1. Ravez, J.; Simon, A. Some Solid State Chemistry Aspects of Lead-Free Relaxor Ferroelectrics. *J. Solid State Chem.* **2001**, *162*, 260–265.
2. Culita, D.C.; Simonescu, C.M.; Patescu, R.E.; et al. Effect of Surfactant Concentration on Textural, Morphological and Magnetic Properties of $CoFe_2O_4$ Nanoparticles and Evaluation of Their Adsorptive Capacity for Pb(II) Ions. *Ceram. Int.* **2015**, *41*, 13553–13560.
3. Li, J.M.; Li, G.Z.; Bai, Z.H.; et al. Effects of Mg Doping on Multiferroic Properties of Bilayered Co1−Mg Fe_2O_4/PMN–PT Composite Thin Films. *Ceram. Int.* **2014**, *40*, 1933–1937.
4. Kolekar, Y.D.; Sanchez, L.; Rubio, E.J.; et al. Grain and Grain Boundary Effects on the Frequency and Temperature Dependent Dielectric Properties of Cobalt Ferrite–Hafnium Composites. *Solid State Commun.* **2014**, *184*, 34–39.
5. Nongjai, R.; Khan, S.; Asokan, K.; et al. Magnetic and Electrical Properties of In Doped Cobalt Ferrite Nanoparticles. *J. Appl. Phys.* **2012**, *112*, 084321.
6. Song, J.; Gao, Y.; Tan, G.; et al. Comparative Study of Microwave Absorption Properties of Ni–Zn Ferrites Obtained from Different Synthesis Technologies. *Ceram. Int.* **2022**, *48*, 22896–22905.
7. Sharma, R.; Thakur, P.; Sharma, P.; et al. Ferrimagnetic Ni Doped Mg-Zn Spinel Ferrite Nanoparticles for High Density Information Storage. *J. Alloys Compd.* **2017**, *704*, 7–17.
8. Šutka, A.; Gross, K.A. Spinel Ferrite Oxide Semiconductor Gas Sensors. *Sens. Actuators B Chem.* **2016**, *222*, 95–105.
9. Oumezzine, E.; Hcini, S.; Baazaoui, M.; et al. Structural, Magnetic and Magnetocaloric Properties of $Zn_{0.6-x}NixCu_{0.4}Fe_2O_4$ Ferrite Nanoparticles Prepared by Pechini Sol-Gel Method. *Powder Technol.* **2015**, *278*, 189–195.
10. Kershi, R.M. Spectroscopic, Elastic, Magnetic and Optical Studies of Nanocrystallite and Nanoferro-Fluids Co Ferrites Towards Optoelectronic Applications. *Mater. Chem. Phys.* **2020**, *248*, 122941.
11. Dhineshbabu, N.R.; Vettumperumal, R.; Narendrakumar, A.; et al. Optical Properties of Lanthanum-Doped Copper Spinel Ferrites Nanoparticles for Optoelectronic Applications. *Adv. Sci. Eng. Med.* **2017**, *9*, 377–383.
12. Khan, A.A.; Javed, H.M.A.; Hussain, S.; et al. Influence of Preparation Method on Structural, Optical and Magnetic Properties of Nickel Ferrite Nanoparticles. *Mater. Sci.-Pol.* **2017**, *35*, 58–65.
13. Zaouali, A.; Maaref, M.A.; Gassoumi, M.; et al. High Electrical Conductivity at Room Temperature of $MnCo_2O_4$ Cobaltite Spinel Prepared by Sol–Gel Method. *J. Mater. Sci. Mater. Electron.* **2021**, *32*, 1221–1232.
14. Huili, H.; Grindi, B.; Viau, G.; et al. Effect of Cobalt Substitution on the Structure, Electrical, and Magnetic Properties of Nanocrystalline $Ni_{0.5}Zn_{0.5}Fe_2O_4$ Prepared by the Polyol Process. *Ceram. Int.* **2014**, *40*, 16235–16244.
15. Bo, L.; Hu, Y.; Zhang, Z.; et al. Efficient Photocatalytic Degradation of Rhodamine B Catalyzed by $SrFe_2O_4$/g-C_3N_4 Composite Under Visible Light. *Polyhedron* **2019**, *168*, 94–100.
16. Mazarío, E.; Herrasti, P.; Morales, M.P.; et al. Synthesis and Characterization of $CoFe_2O_4$ Ferrite Nanoparticles Obtained by an Electrochemical Method. *Nanotechnology* **2012**, *23*, 355708.
17. Thakur, P.; Chahar, D.; Taneja, S.; et al. A Review on MnZn Ferrites: Synthesis, Characterization and Applications. *Ceram. Int.* **2020**, *46*, 15740–15763.
18. Jiménez-Miramontes, J.A.; Domínguez-Arvizu, J.L.; Salinas-Gutiérrez, J.M.; et al. Synthesis, Characterization and Photocatalytic Evaluation of Strontium Ferrites Towards H_2 Production by Water Splitting Under Visible Light Irradiation. *Int. J. Hydrogen Energy* **2017**, *42*, 30257–30266.
19. Chen, Y.; Wu, Q.; Bu, N.; et al. Magnetic Recyclable Lanthanum-Nitrogen Co-Doped Titania/Strontium Ferrite/Diatomite Heterojunction Composite for Enhanced Visible-Light-Driven Photocatalytic Activity and Recyclability. *Chem. Eng. J.* **2019**, *373*, 192–202.
20. Bouzayani, M.M.; Soudani, I.; Abdessalem, M.B.; et al. Electrical Conduction Mechanism and Dielectric Properties of the $KSr_{0.5}Fe_2O_4$ Spinel Ferrite. *J. Mater. Sci. Mater. Electron.* **2024**, *35*, 1256.

21. Massoudi, J.; Dhahri, E.; Khirouni, K.; et al. Magnetocaloric Effect, Dielectric Relaxor Behavior, and Evidence for Direct Magnetodielectric Behavior in $Ni_{0.6}Zn_{0.4}Al_{0.5}Fe_{1.5}O_4$ Ceramics for High-Temperature Applications. *J. Phys. Chem. C* **2022**, *126*, 2857–2867.
22. Cheng, Z.-Y.; Katiyar, R.S.; Yao, X.; et al. Dielectric Behavior of Lead Magnesium Niobate Relaxors. *Phys. Rev. B* **1997**, *55*, 8165–8174.
23. Glinchuk, M.D.; Stephanovich, V.A. Dynamic Properties of Relaxor Ferroelectrics. *J. Appl. Phys.* **1999**, *85*, 1722–1726.
24. García Zaldívar, O.; Peláiz-Barranco, A.; Calderón-Piñar, F.; et al. A Relaxation Model by Using a Relaxation Times Distribution for Relaxor Ferroelectrics. *Scr. Mater.* **2006**, *55*, 927–930.
25. Tang, X.G.; Chew, K.-H.; Chan, H.L.W. Diffuse Phase Transition and Dielectric Tunability of $Ba(Zr_yTi_{1-y})O_3$ Relaxor Ferroelectric Ceramics. *Acta Mater.* **2004**, *52*, 5177–5183.
26. Fang, T.-T.; Chiu, T.-Y. Polarization Dynamics of Polar Nano-Regions in Sr0.5Ba0.5Nb2O6 Doped with Combinations of Ce and Cr. *Acta Mater.* **2011**, *59*, 1692–1699.
27. Wu, C.-C.; Yang, C.-F. Effects of $NaNbO_3$ Concentration on the Relaxor and Dielectric Properties of the Lead-Free $(Na_{0.5}Bi_{0.5})TiO_3$ Ceramics. *CrystEngComm* **2013**, *15*, 9097.
28. Rayssi, C.; El.Kossi, S.; Dhahri, J.; et al. Frequency and Temperature-Dependence of Dielectric Permittivity and Electric Modulus Studies of the Solid Solution $Ca_{0.85}Er_{0.1}Ti_{1-x}Co_{4x/3}O_3$ ($0 \leq x \leq 0.1$). *RSC Adv.* **2018**, *8*, 17139–17150.
29. Smari, M.; Rahmouni, H.; Elghoul, N.; et al. Electric–Dielectric Properties and Complex Impedance Analysis of $La_{0.5}Ca_{0.5-x}Ag_x$ MnO_3 Manganites. *RSC Adv.* **2015**, *5*, 2177–2184.
30. Cai, W.; Fu, C.; Gao, J.; et al. Effect of Hafnium on the Microstructure, Dielectric and Ferroelectric Properties of $Ba[Zr_{0.2}Ti_{0.8}]O_3$ Ceramics. *Ceram. Int.* **2012**, *38*, 3367–3375.
31. Ke, S.; Fan, H.; Huang, H.; et al. Lorentz-Type Relationship of the Temperature Dependent Dielectric Permittivity in Ferroelectrics with Diffuse Phase Transition. *Appl. Phys. Lett.* **2008**, *93*, 112906.
32. Bobić, J.D.; Vijatović Petrović, M.M.; Banys, J.; et al. Electrical Properties of Niobium Doped Barium Bismuth-Titanate Ceramics. *Mater. Res. Bull.* **2012**, *47*, 1874–1880.
33. Massoudi, J.; Bouekkeze, D.; Bougoffa, A.; et al. Structural, Elastic, Optical and Dielectric Properties of $Li_{0.5}Fe_{2.5}$ O_4 Nanopowders with Different Particle Sizes. *Adv. Powder Technol.* **2020**, *31*, 4714–4730.
34. Kubelka-Munk Equation. *Springer Reference*; Springer: Berlin/Heidelberg, Germany, 2011.
35. Tauc, J.; Menth, A. States in the Gap. *J. Non-Cryst. Solids* **1972**, *8–10,* 569–585.
36. Hadded, A.; Massoudi, J.; Dhahri, E.; et al. Structural, Optical and Dielectric Properties of $Cu_{1.5}Mn_{1.5}O_4$ Spinel Nanoparticles. *RSC Adv.* **2020**, *10*, 42542–42556.
37. Soudani, I.; Massoudi, J.; Smari, M.; et al. Research on the Physical Properties of $LiMn_{0.5}Fe_2O_4$ Spinel Ferrites by the Combination of Optical, Magnetic, and Dielectric Behaviors. *RSC Adv.* **2023**, *13*, 9260–9272.
38. Soudani, I.; Weslati, N.; Znaidia, S.; et al. An Experimental Investigation of Vibrational, Optical, and Dielectric Properties of Li–Mg Ferrite for Potential High-Frequency and Optoelectronic Applications. *RSC Adv.* **2025**, *15*, 26873–26885.
39. Kalyanaraman, S.; Shajinshinu, P.M.; Vijayalakshmi, S. Determination of Optical Constants and Polarizability Studies on Ferroic Tetramethylammonium Tetracholorozincate Crystal. *Phys. B Condens. Matter* **2016**, *482*, 38–42.
40. Souissi, H.; Taktak, O.; Khalfa, M.; et al. Experimental and Optical Studies of the New Organic Inorganic Bromide: $[(C_3H_7)_4N]_2CoBr_4$. *Opt. Mater.* **2022**, *129*, 112513.
41. Mnakri, M.; Gharbi, I.; Enneffati, M.; et al. Synthesis and Investigation on the Optical and Complex Impedance Analysis in $LiCrO_2$ Prepared Using Solid-State Reaction. *Mater. Today Commun.* **2024**, *38*, 107714.